Multicontrol Surface Optimization for Blended Wing–Body Under Handling Quality Constraints

Yann Denieul, Joël Bordeneuve-Guibé, Daniel Alazard, Clément Toussaint, Gilles Taquin

Multicontrol Surface Optimization for Blended Wing–Body Under Handling Quality Constraints

Yann Denieul,* Joël Bordeneuve,† and Daniel Alazard‡
ISAE-SUPAERO, University of Toulouse, 31055 Toulouse, France
Clément Toussaint§
ONERA—The French Aerospace Lab, 31055 Toulouse, France
and
Gilles Taquin¶
Airbus Opérations SAS, 31060 Toulouse, France

DOI: 10.2514/1.C034268

Control architecture sizing is a main challenge of blended-wing–body design. This aircraft configuration typically features redundant elevons located at the trailing edge of the wing, acting simultaneously on pitch and roll axes. Consequently, a proper sizing requires one to consider coupled longitudinal and lateral criteria. Moreover, significant hinge moments due to large control surface areas, combined with high deflection rates in order to safely control the longitudinal instability, may result in excessive power consumption and actuator mass penalty. Therefore, it is highly desirable at the preliminary design level to minimize control surface areas, while ensuring adequate closed-loop handling qualities, with limited deflections and deflection rates. The problem of integrated design of control surface sizes and flight control laws for an unstable blended-wing–body aircraft is addressed here. The latest tools for H_∞ nonsmooth optimization of structured controllers are used to optimize in a single step the gains for both longitudinal and lateral control laws, as well as a control allocation module, while minimizing the control surface span. The following constraints are ensured: maximal deflection angles and rates for 1) pilot longitudinal pull up, 2) pilot bank angle order, and 3) longitudinal turbulence. Using this coupled approach, significant gains in terms of the outer elevon's span as compared to the initial layout are demonstrated, whereas closed-loop handling quality constraints are guaranteed.

Nomenclature

n_{controls}	=	number of control surfaces
$y_{2_{\text{inb}}}$	=	inboard y position of elevon 2
$y_{5_{\text{out}}}$	=	outboard y position of elevon 5
$y_{2_{\text{inb}}}^{\text{init}}$	=	initial inboard y position of elevon 2
$y_{5_{\text{out}}}^{\text{init}}$	=	initial outboard y position of elevon 5

I. Introduction

AMONG other disruptive aircraft configurations, the blended-wing–body (BWB) has been considered for years as a promising candidate for the future of civil aviation [1]. The rationale for this game-changing configuration is as follows: instead of considering separate geometrical components for each basic function of an aircraft (namely, lift, transport, control, and propulsion), the BWB gathers the three functions of lift, transport, and control into a single lifting surface. As a consequence of merging these functions, an overall improved efficiency is expected, involving significant gains in terms of fuel consumption. Most gains come from a decreased wetted area as compared to a classical tube-and-wing design; but, also, structural mass improvements are expected. As a result, studies from the literature have regularly forecast gains ranging from 15 to 20% in terms of fuel consumption as compared to a conventional configuration [1–4]. This paper focuses on an Airbus long-range BWB configuration.

Major challenges are yet to be solved before a potential entry into service, including control-related issues [5]. These issues first originate from the nature of the control devices used for this configuration: the BWB (also known in the literature as hybrid wing–body [6]) is controlled with multicontrol surfaces (also named elevons), usually spanning the whole trailing edge and acting as pitch and roll devices. Among the challenges associated with this technology, new handling quality criteria are required in order to take into account the combined authority of control surfaces on longitudinal and lateral axes. This was already addressed in previous work [7,8]. Then, these control surfaces typically lack longitudinal pitch authority because of their small longitudinal lever arm as compared to that of a conventional elevator.

Flight control system (FCS) sizing is also affected by these unusual effectors: failure cases of actuators or control surfaces induce a loss of authority on both pitch and roll axes. The failure case analysis then tends to be more complex than for classical aircraft configurations, where functions are segregated for each axis. However, we will make the assumption that a failure case analysis sizes the number of redundant elevons and the number of actuators per elevon [9] rather than the elevon's total area, which is the main concern of this paper. Failure scenario analyses for elevon layout sizing, which were already addressed by Garmendia et al. [10] and in the Active Control for Flexible 2020 Aircraft 2020 studies [11], are therefore outside the scope of our study.

Then, concerning control surface area sizing, two phenomena have a combined detrimental effect on both the actuator mass and power consumption:

1) On the one hand, trailing-edge elevons induce high aerodynamic hinge moments (HMs) due to their large area [12]. It has been known since the work of Roman et al. [5] that hinge moments are related to the control surface area through a "square-cube" law: control surface areas increase as the square of the scale λ^2, whereas hinge moments increase with the cube of this scale λ^3. Large BWB control surfaces lead to high hinge moment requirements. Moreover, the control surface's inertia is proportional to $\lambda^{5/2}$.

Presented as Paper 2015-2553 at the AIAA Atmospheric Flight Mechanics Conference, Dallas, TX, 22–26 June 2015; received 5 November 2016; revision received 24 June 2017; accepted for publication 12 July 2017; published online 29 August 2017.

*Ph.D. Student, 10, Av. Edouard Belin. Student Member AIAA.
†Professor, 10, Av. Edouard Belin.
‡Professor, 10, Av. Edouard Belin. Member AIAA.
§Research Engineer, 2, Av. Edouard Belin.
¶Handling Qualities Expert, Future Projects Office, 316 route de Bayonne.

From this perspective, during the preliminary design phase, attention should be focused on downsizing the control surface areas.

2) On the other hand, high deflection rates result from the longitudinal stabilization of an unstable configuration [13]. Indeed, the Airbus BWB features a negative static margin, especially at low speed (see Sec. II.B). Otherwise said, our aircraft features an unstable short-period mode. For this reason, it requires a permanent stability augmentation system (SAS) in order to guarantee adequate safety and handling qualities. However, it was shown in a previous study [14] that, the more unstable an aircraft, the faster its control surfaces need to move in order to maintain the equilibrium under disturbance. This effect is further increased on the BWB because elevons lack a longitudinal lever arm with respect to the center of gravity (CG). As a consequence, their longitudinal efficiency is reduced as compared to an elevator of the same area on a conventional airplane. Thus, more demanding deflections and deflection rates are needed to create the same pitching moment. As a result, deflection rates of 60 deg/s [15] and even 100 deg/s [16] are often considered when presizing the FCS for a BWB, as compared to nominal values of about 30 deg/s for conventional tail-aft design actuators. During the preliminary design phase, control surface pitch efficiency should then be sought to be maximized (for instance, by increasing the control surface area as much as possible), which conflicts with the previously mentioned requirement on hinge moment limitation.

Both large hinge moments and high deflection rates have a direct impact on the FCS sizing and secondary power consumption. Indeed, as stated by Garmendia et al. [17], secondary power for the FCS P_{FCS} may be evaluated in a preliminary way by Eq. (1):

$$P_{\text{FCS}} = \sum_{i=1}^{n_{\text{controls}}} \text{HM}_i^{\max} \cdot \dot{\theta}_i^{\max} \tag{1}$$

where $\text{HM}_i^{\max}$ and $\dot{\theta}_i^{\max}$ are the maximum hinge moment and maximum deflection rate of the ith control surface, respectively; and n_{controls} is the number of control surfaces.

At the preliminary design phase, when the actuator's sizing is not yet frozen, the deflection rate is a direct consequence of the control law design. Also, the traditional way of sizing conventional control surfaces considers simplified open-loop handling qualities criteria, such as the roll rate target for the ailerons or the pitch rate target for the elevator. Such an approach is no longer valid for BWB control surface sizing due to the natural pitch instability: control surface areas may be largely sized by stabilization requirements, so sizing requires considering control laws at the early design phase. Control law design in turn depends on the effectiveness of control surfaces. This coupled problem is known in the control community as plant-controller optimization or integrated design and control. The classical way of handling this problem involves an iterative approach: effectors are sized based on engineering rules, and then a control law is designed. If the requirements are not met, then the sizing is changed based on the existing control law, and so on. However, it has been proved [18] that, in addition to being time-consuming, this approach may miss the optimum because of the tightly coupled nature of the problem. Consequently, several approaches seek to solve these combined problems in a single step. "Plant-controller optimization" has been studied in a variety of fields, such as chemistry [19,20], autonomous underwater vehicles [21], and astronautics [14,22,23].

In the field of aeronautics, two complementary approaches were studied. The first method considered integrating a stability and control module into a multidisciplinary optimization (MDO) process [24,25]. Longitudinal and lateral control laws were synthesized using a linear quadratic technique, and they were incorporated into an optimization process, together with an aerodynamics, propulsion, weight, and performance module. Optimization was run with and without taking into account the stability augmentation system for a conventional tail-aft design. The results showed improved performance for the relaxed static stability due to smaller elevator sizing. Other MDO studies also considered stability constraints for BWB planform optimization [26–28].

A second, more control-oriented approach takes advantage of optimization tools developed for controller design in order to simultaneously optimize a controller and some meaningful physical parameters. Niewhoener and Kaminer [29] optimized, in a single loop, a longitudinal controller and elevator control surface using a linear matrix inequality (LMI) framework. The handling quality constraints were expressed in terms of the LMI. The resulting controller was full order. This approach was later developed in other studies of integrated longitudinal controller/control surface sizing [30,31] and design of hypersonic vehicles [32]. More recently, nonsmooth optimization methods enabling structured linear varying parameter (LPV) controllers were applied to the longitudinal integrated design and control problem [33].

We propose to extend this approach to longitudinal/lateral integrated design and control of a BWB by optimizing together a three-axis control law and a control surface total span, using nonsmooth optimization techniques for fixed structure controllers. More precisely, we propose to optimize in a single step the control surface span, the control allocation module, and the flight control laws in order to guarantee longitudinal and lateral handling quality constraints with a minimum control surface size. The main contributions of this paper as compared to the state-of-the-art literature are threefold: 1) applying the methodology of integrated design and control to a BWB, 2) extending the plant-controller optimization problem to a coupled longitudinal/lateral case, and 3) using optimization tools for fixed-structured controllers in order to solve this problem.

This paper is organized as follows: in Sec. II, the flight dynamics models are presented. Then, Sec. III introduces the strategy for parameterizing the elevon's total span and obtaining a parametrized state-space representation suitable for optimization. The integrated design and control problem of computing structured longitudinal/lateral control laws gains together with optimal elevons size is presented in Sec. IV, and the results are discussed in Sec. V.

II. Aircraft Flight Dynamics and Control

In this section, the models used in Secs. III and IV for design, control, and simulation are described. The configuration studied in this paper is a long-range BWB for which the planform results from optimization studies on high-speed performance with constraints on the low-speed pitching moment [34]. The focus of this work is the sizing of control surfaces; thus, the planform is considered constant. The planform and initial control surface layout are visible on Fig. 1a.

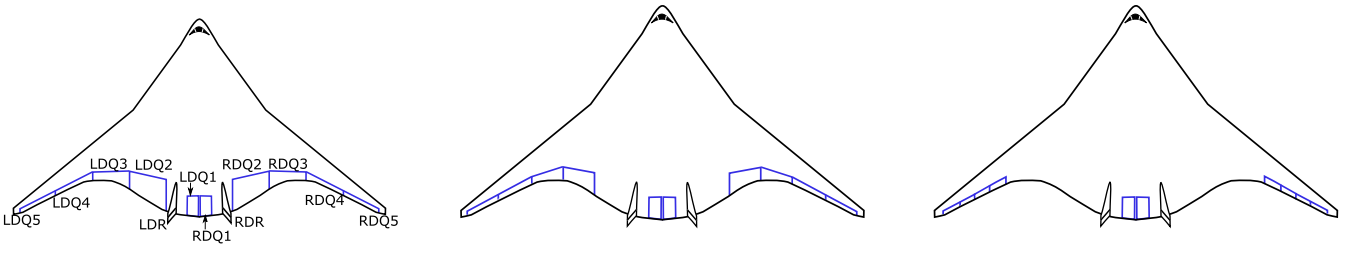

a) $\eta = 1$ **b) $\eta = 0.8$** **c) $\eta = 0.4$**

Fig. 1 Elevon sizes for different values of parameter η.

A. Linearized State-Space Representation of Flight Dynamics Equations

This work focuses on the elevon's sizing based on closed-loop longitudinal and lateral handling qualities criteria. Consequently, three-axis nonlinear flight dynamics equations are used to simulate the aircraft motion. Using Newton's second law,

$$m\dot{\boldsymbol{V}}_g = m\boldsymbol{g} + \boldsymbol{F}_{\text{aero}} + \boldsymbol{F}_{\text{thrust}} \tag{2}$$

$$\boldsymbol{J}\dot{\boldsymbol{\Omega}}^G = \boldsymbol{M}^G_{\text{aero}} + \boldsymbol{M}^G_{\text{thrust}} \tag{3}$$

where m and $\boldsymbol{J}$ are the aircraft mass and inertia, respectively; $\boldsymbol{V}_g$ is the ground speed; $\dot{\boldsymbol{V}}_g$ is its derivative with respect to the $R_0(x_0, y_0, z_0)$ Earth reference frame; and $\boldsymbol{\Omega}^G$ is the aircraft rotation vector around its center of gravity. $\boldsymbol{F}_{\text{aero}}$ and $\boldsymbol{M}^G_{\text{aero}}$ denote the aerodynamic forces and moments, respectively; whereas $\boldsymbol{F}_{\text{thrust}}$ and $\boldsymbol{M}^G_{\text{thrust}}$ are the forces and moments resulting from engine thrust, respectively. For an extensive development of these equations, the reader may refer to [35].

To perform the control law synthesis and linear analysis, these equations are linearized around equilibrium flight points. These initial equilibria are computed for the following conditions: zero flight-path angle, sideslip, and bank angle. The choice of different flight points in terms of mass, Mach, and altitude is discussed in Sec. II.E. The following state-space representation was used:

$$\begin{bmatrix} \delta\dot{V} \\ \delta\dot{\alpha} \\ \dot{q} \\ \delta\dot{\theta} \\ \dot{\beta} \\ \dot{r} \\ \dot{p} \\ \dot{\phi} \end{bmatrix} = \underbrace{\begin{bmatrix} x_V & x_\alpha & x_q & -g & x_\beta & 0 & 0 & 0 \\ -z_V & -z_\alpha & 1-z_q & 0 & 0 & 0 & 0 & 0 \\ 0 & m_\alpha & m_q & 0 & 0 & 0 & 0 & 0 \\ 0 & 0 & 1 & 0 & 0 & 0 & 0 & 0 \\ 0 & 0 & 0 & 0 & y_\beta & y_r - \cos\alpha & y_p + \sin\alpha & \frac{g\cos\theta}{V_e} \\ 0 & 0 & 0 & 0 & \tilde{n}_\beta & \tilde{n}_r & \tilde{n}_p & 0 \\ 0 & 0 & 0 & 0 & \tilde{l}_\beta & \tilde{l}_r & \tilde{l}_p & 0 \\ 0 & 0 & 0 & 0 & 0 & \tan\theta & 1 & 0 \end{bmatrix}}_{\text{State matrix } A} \underbrace{\begin{bmatrix} \delta V \\ \delta\alpha \\ q \\ \delta\theta \\ \beta \\ r \\ p \\ \phi \end{bmatrix}}_{\text{States } X}$$

$$+ \underbrace{\begin{bmatrix} x_{\delta x} & x_{\delta m_i} & 0 \\ 0 & -z_{\delta m_i} & 0 \\ 0 & m_{\delta m_i} & 0 \\ 0 & 0 & 0 \\ 0 & y_{\delta m_i} & y_{\delta n} \\ 0 & \tilde{n}_{\delta m_i} & \tilde{n}_{\delta n} \\ 0 & \tilde{l}_{\delta m_i} & \tilde{l}_{\delta n} \\ 0 & 0 & 0 \end{bmatrix}}_{\text{Control effectiveness matrix } B} \underbrace{\begin{bmatrix} \Delta\delta x \\ \Delta\delta m_i \\ \delta n \end{bmatrix}}_{\text{Controls } U} + \underbrace{\begin{bmatrix} 0 \\ \frac{-z_\alpha}{V_e} \\ 0 \\ \vdots \\ 0 \end{bmatrix}}_{\text{Gust disturbance matrix } B_w} w_z \tag{4}$$

$$\underbrace{\begin{bmatrix} X \\ \delta Nz \end{bmatrix}}_{\text{Outputs } Y} = \begin{bmatrix} 1 & 0 & \cdots & & 0 \\ 0 & \ddots & & & \vdots \\ \vdots & & & 1 & 0 \\ 0 & & \cdots & 0 & 1 \\ \frac{V_e}{g} z_V & \frac{V_e}{g} z_\alpha & \frac{V_e}{g} z_q & 0 \cdots & 0 \end{bmatrix} X + \begin{bmatrix} 0 \\ \vdots \\ 0 \\ z_{\delta m_i} \end{bmatrix} \Delta\delta m_i + \begin{bmatrix} 0 \\ \vdots \\ 0 \\ \frac{z_\alpha}{g} \end{bmatrix} w_z \tag{5}$$

where $X = [\delta V \quad \delta\alpha \quad q \quad \delta\theta \quad \beta \quad r \quad p \quad \phi]^T$ is the state vector composed of $\delta V = V - V_e$, which is the relative airspeed with respect to the equilibrium speed; $\delta\alpha = \alpha - \alpha_e$ and $\delta\theta = \theta - \theta_e$ are the relative angle of attack and pitch attitude with respect to the equilibrium, respectively; sideslip is β; and p, q, and r are the rotation rates of the aircraft with respect to the Earth reference frame in roll, pitch, and yaw, respectively. Comprehensive expressions of the matrix coefficients are given in the Appendix. The controls are $\Delta\delta x = \delta x - \delta x_e$, which is the relative symmetric thrust with respect to the equilibrium thrust; and $\Delta\delta m_i = \delta m_i - \delta m_e$, $i = 1, \ldots, 10$, is the relative deflection of the ith elevon control surface with respect to the equilibrium position. Elevons for the BWB are acting not only for maneuvers but also as trim devices. Equilibria for this study were performed using all elevons with equal deflection. Other studies showed the benefits of segregating trim and maneuver control surfaces [6], but this trade is out of the scope of our work. However, for maneuvers, each of the 10 elevons is actuated independently, through a control allocation strategy presented in Sec. IV.B. The elevon's layout, shown in Fig. 1a, is ordered in the control vector as follows:

$$\delta m_{i,i=1,\ldots,10} = [\text{LDQ1} \ldots \text{LDQ5}, \text{RDQ1} \ldots \text{RDQ5}]$$

The control vector also contained the rudder deflection δn. Although two rudders are visible on the configuration of Fig. 1a, it was chosen for the sake of clarity to group them as a single control with twice the efficiency of one rudder; the aim of our study is, indeed, not to size vertical surfaces, but only elevons. The output vector Y gathers the aircraft states and vertical load factor $\delta Nz = Nz - 1$, with the vertical load factor for the initial equilibrium being equal to one. Finally, a turbulence effect is included as a vertical velocity w_z expressed in the Earth reference frame, under the assumption that it acts as an increment of angle of attack. The model used for turbulence is described in Sec. II.C.

B. Mode Analysis

The modes of the eight-state aircraft dynamics presented in Sec. II.A are depicted in Fig. 2. For the sake of clarity, poles are shown only for one mass and altitude, with the Mach number varying between 0.45 to 0.85. More generally, all of this work is performed for the

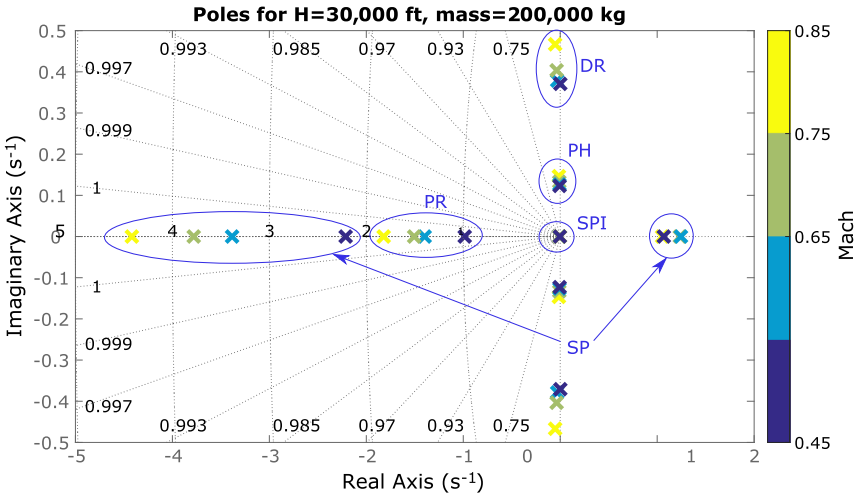

Fig. 2 Poles of aircraft dynamics for aft CG (PR denotes pure roll, PH denotes phugoid mode, and SPI denotes spiral mode).

maximum aft CG allowed for each mass in order to be at the most penalizing configuration from a longitudinal stability perspective.

The main point to retain from Fig. 2 is the strong instability of the short-period oscillation, with a frequency of approximately 1.2 rad $\cdot$ s^{-1}. Even though it is not comparable to the most unstable fighter aircraft ever designed, such as the X-29 (see [36], with instability levels approaching 6 rad $\cdot$ s^{-1}), this instability level is an order of magnitude beyond current civil aircraft: these are currently designed to be at least neutrally stable in an open loop. Identifying and minimizing the impact of this unstable mode on control surface sizing are the main concerns of this paper.

In Fig. 2, a poorly damped Dutch roll (DR) mode is also visible. For some flight points, it even turns slightly unstable. A previous study [7] sized the vertical surfaces of this configuration in order to guarantee a minimum instability level of $\xi = -5\%$ for the Dutch roll on the whole flight envelope.

C. Turbulence Model

A Dryden continuous turbulence model is used for simulating vertical continuous turbulence w_z. A band-limited white noise e_z is passed through a forming filter approximating the Dryden velocity spectra. The transfer function has the following expression from [37]:

$$H_{w_z}(s) = \frac{w_z}{e_z}(s) = \sigma_z \sqrt{\frac{2L_z}{\pi V}} \frac{1 + (\sqrt{3}L_z/V)s}{(1 + (L_z/V)s)^2} \tag{6}$$

where V is the aircraft airspeed, and L_z is the vertical turbulence scale length that was set to 500 m. This value is typical from [38] for simulating turbulence at altitudes above 2000 ft. Note that σ_z is the turbulence intensity; in this work, the value $\sigma_z = 5$ m $\cdot$ s^{-1} is chosen in order to simulate severe turbulence intensity. The underlying rationale for this choice is that we should size control surfaces in order to guarantee a stable closed-loop behavior, even for extreme turbulence events. For an unstable aircraft such as the BWB studied here, if the deflection stops or rate limits of the actuators are reached during stabilization, then the aircraft dynamics may revert back to an unstable behavior. This may lead to the aircraft loss. Thus, extreme turbulence was chosen for control surface sizing.

D. Actuator Model

A second-order actuator model accounting for their bandwidth and damping is used:

$$\frac{y_{\text{act}}}{u_{\text{act}}} = \frac{\omega_0^2}{s^2 + 2\xi\omega_0 s + \omega_0^2} \tag{7}$$

A single bandwidth and damping of, respectively, $\omega_0 = 8.8$ rad $\cdot$ s^{-1} (1.4 Hz) and $\xi = 0.8$ was used. Previous studies considered allocating different bandwidths for all control surfaces [14,39]; however, this is outside the scope of the present paper. A 100 ms delay accounting for sensors, computers, and data processing is included in the control law synthesis and simulation. Such a value is typical for an actual control chain delay; challenging the current technology would, of course, improve the control law performance but is not considered here. During synthesis on the linearized model, a second-order Padé approximation is used; for simulation, the actual delay is taken into account. Actuators and delay will be embedded in the control law structure in Sec. IV.C.

E. Description of the Flight Envelope

To properly size the aircraft from a stability and control perspective, our integrated design and control process was run on the entire flight envelope in terms of mass, Mach, altitude, and for aft CG. More precisely, four masses were examined: $m = [200T, 250T, 300T, 350T]$. Mach numbers were discretized from 0.25 to 0.85 with steps of 0.1; for each Mach number, a sweep was performed on the airspeed V_{air} with steps of 20 kt. This is equivalent to varying the altitude for a given Mach. Admissible altitudes were given by a velocity maximum operating limitation for the low-altitude limit and a maximum of the buffet lift coefficient and operational ceiling for the high-altitude limit. The resulting flight points are depicted in Fig. 3.

III. Parametric Representation of Control Surface Span Variation

In this section, a process for obtaining a continuous approximation of control surface efficiencies for varying the outer elevon's span is presented. This part aims at obtaining a continuously parametrized state-space representation so that the continuous optimizer presented

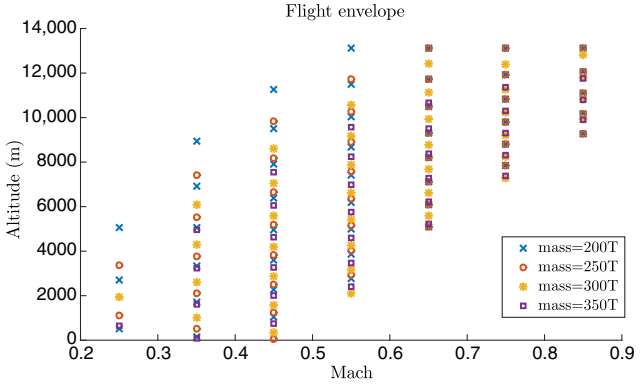

Fig. 3 Mach–altitude flight envelope.

in Sec. IV may use the continuous variable representing the elevon's size as an optimization variable.

A. Geometric Parametrization of Control Surfaces Span

In "classical" plant-controller optimization problems applied to aeronautics, attention is drawn to minimizing the elevator size under longitudinal constraints. For the BWB lacking (by definition) an elevator, this process is not applicable here. Therefore, the outer elevon's total span is chosen as a plant figure of merit to be minimized. More precisely, a variable η representing the ratio of the outer elevon's total span as compared to the initial control surface's span is introduced. In Fig. 1a, the initial elevon's layout, corresponding to a parameter value of $\eta = 1$, is presented. This initial layout features five control surfaces on each side of the wing spanning the whole trailing edge, except a gap between elevons 1 and 2 for engine pylon integration: elevons are numbered from inboard to outboard. The elevon's relative chord is limited in the x-wise position by cabin integration for elevon 1, and by the rear spar for elevons 2 to 5. So, it was decided to keep the elevon's relative chord constant, as well as the elevon's number; as mentioned in the Introduction (Sec. I), the elevon's number is mostly a failure case problem that is out of the scope of our study. Also, the initial elevons are split equally on the outer wing; that is, elevons 2 to 5 have the same span.

From this initial layout, control surfaces were derived using the following assumptions:

1) Note that $\eta = (y_{2_{\text{inb}}}/y^{\text{init}}_{2_{\text{inb}}})$, $y_{2_{\text{inb}}}$ and $y^{\text{init}}_{2_{\text{inb}}}$ are the current and the initial inboard y position of elevon 2, respectively.

2) Note that $y_{5_{\text{out}}} = y^{\text{init}}_{5_{\text{out}}}$, $y_{5_{\text{out}}}$ and $y^{\text{init}}_{5_{\text{out}}}$ are the current and the initial inboard y position of elevon 5, respectively.

3) The elevon's relative chords are kept constant and equal to 22%.

4) Elevons 2 to 5 are split equally.

5) Elevon 1 is kept constant.

It is then clear that $0 \leq \eta \leq 1$, $\eta = 1$, corresponding to an initial elevon's layout, and $\eta = 0$, corresponding to the lack of any control surface on the outer wing. Examples of layouts for $\eta = 0.8$ and $\eta = 0.4$ are presented on Figs. 1b and 1c, respectively.

B. Computation of Aerodynamic Models for Discretized Control Surface Span

The computation of an aerodynamic model for different parameter values of η is described in this section. For the sake of clarity, the initial layout (namely, the configuration for $\eta = 1$) is called the "reference" aircraft; whereas derived layouts (namely, configurations for $\eta < 1$) are called "project" aircraft. The reference flight dynamics model described in Sec. II.A is used for all configurations described in Sec. III.A as a planform, and airfoils are kept constant for all configurations; therefore, only control surface aerodynamic efficiencies need to be evaluated for the project aircraft. Once again, the goal of Sec. III is to obtain state-space representations continuously parametrized by elevon span parameter η. The process to obtain such a continuous approximation is presented in Fig. 4. A first step is to compute calibrated aerodynamic models for discrete values of η, namely, for values between 0.1 and 1, with steps of 0.1. For that purpose, the Athena Vortex Lattice (AVL) software [40] was used together with calibration factors coming from the supposedly known aerodynamic coefficients of the initial BWB design. This allows one to take into account the Mach effects and nonlinearities due to a high angle of attack or high deflection, which AVL cannot account for. Continuous approximation of discretized models is treated in Sec. III.C, whereas computation of calibrated aerodynamic models is explained hereafter.

More precisely, the aircraft total lift coefficient C_L embedded in the F_{aero} term of Eq. (3) comprises an ith control surface deflection dependency C_{L_i}, which can be written as follows:

$$C_{L_i} = k^{\text{NL}}_{\delta m_i}(\alpha, \delta m_i) C_{L_{\delta m_i}} \delta m_i \tag{8}$$

where $k^{\text{NL}}_{\delta m_i}(\alpha, \delta m)$ accounts for loss-of-control surface efficiency as a function of the angle of attack α and control surface deflection δm_i, and $C_{L_{\delta m_i}}$ is the lift gradient of the ith control surface. Note that $k^{\text{NL}}_{\delta m_i}(\alpha, \delta m)$ is known for reference aircraft, and it is kept for project aircraft. The reference lift gradient $C^{\text{ref}}_{L_{\delta m_i}}$ is supposed known from previous studies [34], and it is compared with the lift gradient computed by AVL for the reference configuration $C^{\text{AVL}}_{L_{\delta m_i}}$ (see Fig. 5a). From these data, a calibration factor accounting for AVL's lack of accuracy is computed:

$$\Delta C^{\text{AVL}}_{L_i} = \frac{C^{\text{ref}}_{L_{\delta m_i}}}{C^{\text{AVL}}_{L_{\delta m_i}}} \tag{9}$$

Then, an AVL computation is run on project geometry in order to compute the lift gradient of the project aircraft $C^{\text{AVL}^{\text{proj}}}_{L_{\delta m_i}}$. This gradient is finally calibrated using the previously computed calibration factor $\Delta C^{\text{AVL}}_{L_i}$ of Eq. (9) (see Fig. 5b), giving the following:

$$C^{\text{proj}}_{L_i} = k^{\text{NL}}_{\delta m_i} \Delta C^{\text{AVL}}_{L_i} C^{\text{AVL}^{\text{proj}}}_{L_{\delta m_i}} \delta m_i \tag{10}$$

A similar process is used for computing the control surface's pitching moment efficiencies of project configurations. More precisely, the aircraft pitching moment coefficient C_m embedded in $\boldsymbol{M}^G_{\text{aero}}$ of Eq. (3) comprises an ith control surface deflection dependency C_{m_i}, which can be written as follows:

$$C_{m_i} = k^{\text{NL}}_{\delta m_i}(\alpha, \delta m_i) C_{L_{\delta m_i}} \delta m_i (X_{\text{CG}} - X_{F_i}) \tag{11}$$

where X_{CG} denotes the x-wise CG position, and X_{F_i} denotes the ith control surface aerodynamic center x-wise position. However, X_{F_i} is not a direct output of AVL and has to be computed as follows:

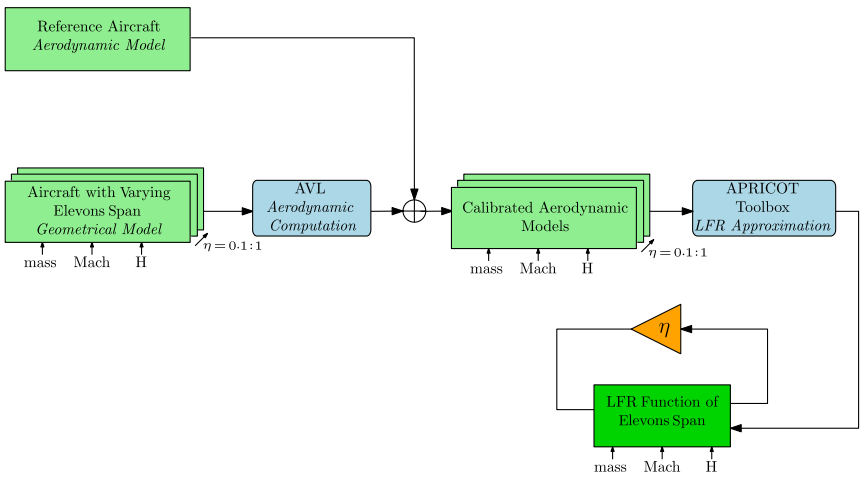

Fig. 4 Process for obtaining LFR approximation of state-space representations as a function of the η parameter.

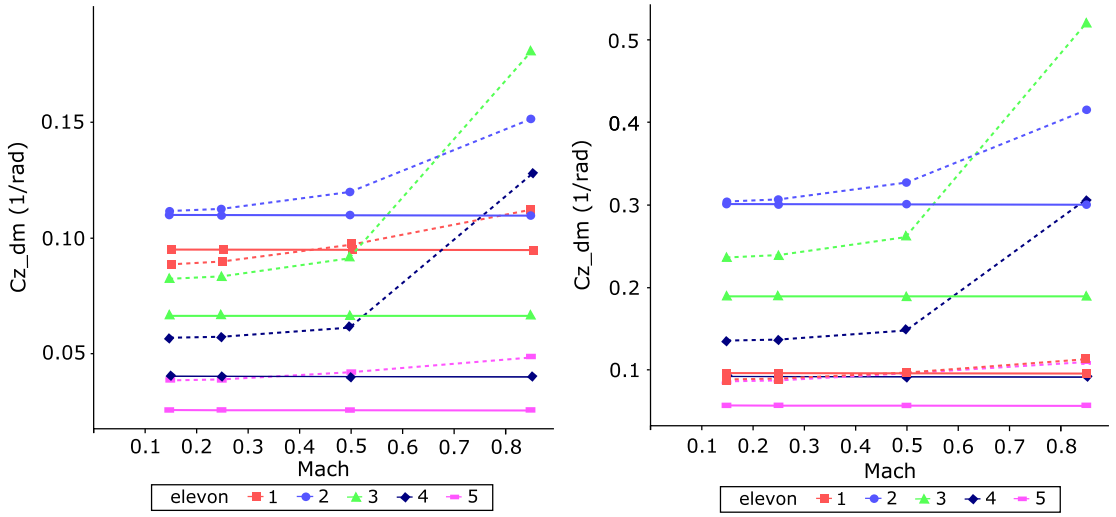

a) Comparison of lift gradient coefficients for reference aircraft: $C^{ref}_{L\delta m_i}$ (dotted) vs $C^{AVL}_{L\delta m_i}$ (plain)

b) Comparison of lift gradient coefficients for project aircraft before (plain) and after calibration (dotted), respectively

Fig. 5 Comparison of AVL outputs with reference aircraft aerodynamic data (left) and with calibrated data (right).

$$X^{\text{AVL}}_{F_i} = X_{\text{CG}} - \frac{C^{\text{AVL}}_{m_{\delta m_i}}}{C^{\text{AVL}}_{L_{\delta m_i}}} \tag{12}$$

This leads to computing the aerodynamic center calibration factor for the reference aircraft, knowing the actual aerodynamic center $X^{\text{ref}}_{F_i}$ for the ith elevon:

$$\Delta X^{\text{AVL}}_{F_i} = \frac{X^{\text{ref}}_{F_i}}{X^{\text{AVL}}_{F_i}} \tag{13}$$

Finally, an AVL computation is run on project aircraft in order to compute the pitching moment gradient of the project aircraft's ith elevon $C^{\text{AVL}^{\text{proj}}}_{m_{\delta m_i}}$, and the resulting aerodynamic center is computed and calibrated as follows:

$$X^{\text{AVL}^{\text{proj}}}_{F_i} = \Delta X^{\text{AVL}}_{F_i} \cdot \left(X_{\text{CG}} - \frac{C^{\text{AVL}^{\text{proj}}}_{m_{\delta m_i}}}{C^{\text{AVL}^{\text{proj}}}_{L_{\delta m_i}}} \right) \tag{14}$$

A similar process is used for computing the control surface's rolling moment efficiencies of project configurations. More precisely, the aircraft rolling moment coefficient C_l embedded in M^G_{aero} of Eq. (3) comprises an ith control surface deflection dependency C_{l_i}, which can be written as follows:

$$C_{l_i} = k^{\text{NL}}_{\delta m_i}(\alpha, \delta m_i) C_{l_{\delta m_i}} \delta m_i \tag{15}$$

The calibration factor for the rolling moment coefficient is then computed as follows:

$$\Delta C^{\text{AVL}}_{l_i} = \frac{C^{\text{ref}}_{l_{\delta m_i}}}{C^{\text{AVL}}_{l_{\delta m_i}}} \tag{16}$$

And, finally, the rolling moment coefficient of the project aircraft is calibrated using the calibration factor of Eq. (16):

$$C^{\text{proj}}_{l_i} = k^{\text{NL}}_{\delta m_i} \Delta C^{\text{AVL}}_{l_i} C^{\text{AVL}^{\text{proj}}}_{l_{\delta m_i}} \delta m_i \tag{17}$$

This method, summarized in Fig. 4, combines the advantages of fast data generation through a light computational fluid dynamics computation, and with far better accuracy than AVL direct output through accurate knowledge on a reference configuration. Here, it is applied only to control surface aerodynamic coefficients, but the process would be similar for computing any aerodynamic coefficient of a project aircraft with a baseline knowledge on a similar reference aircraft.

C. Polynomial Approximation and LFR Representation of Control Surface Aerodynamic Efficiencies

Once aerodynamic coefficients are computed and calibrated for discretized values of η (namely, $\eta = [0.1, 0.2, \ldots, 1]$; see Sec. III.B), the final step concerning the modeling problem consists of obtaining an approximation of state-space representations for the continuously varying parameter η. For that purpose, it was chosen to work with the linear fractional representation (LFR) framework because this representation is suited to the optimizer coming from the control community presented in Sec. IV. Moreover, efficient algorithms for approximating a set of numerical data as an LFR were developed by ONERA—The French Aerospace Lab [41]. A LFR is a model where all fixed dynamics are gathered in a single linear time-invariant plant M, whereas uncertainties or varying parameters are contained in a block-diagonal matrix Δ (see Fig. 6). Polynomial and rational expressions are, for instance, easily convertible into a LFR. For a comprehensive LFR theory, please refer to [42].

More precisely, the problem is that of finding a LFR approximating as closely as possible the state-space representations computed for different values of η. Uncertainties are not considered in this study, so the Δ block is only composed of the η parameter repeated several times. Moreover, as mentioned previously, in this work, the BWB planform is kept constant; therefore, state matrix A from the state-space representation is assumed to be independent from η. As a consequence, only control matrix B containing the elevon's efficiencies is approximated by the LFR. However, the described

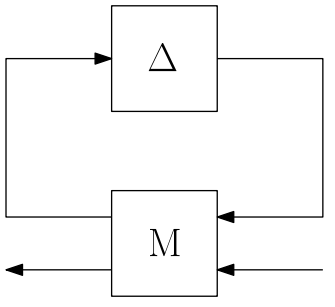

Fig. 6 Linear fractional representation.

process would be similar if we would include some planform variables having an impact on the A matrix.

It was decided to restrict the search for LFR approximations to polynomial approximations in order to keep the LFR order (that is, the amount of times η is repeated inside the Δ block) as small as possible. From a physical perspective, this can be justified by the fact that control surface efficiencies should vary smoothly with respect to their span. The least-squares routine `lsapprox` from the APRICOT library in MATLAB [41] was used. The problem consists of finding a polynomial $\boldsymbol{P}$ of degree n_p minimizing the following criterion:

$$C = \sum_{k=1}^{N} [\boldsymbol{B}_{\eta_k} - \boldsymbol{P}(\eta)]^2 \tag{18}$$

with $\boldsymbol{B}_{\eta_k}$ being the control matrix for sampled values of η, $\eta_{k,k=1:N} = [0.1, \ldots, 1]$.

The degree of the polynomial $\boldsymbol{P}$ is set to $n_p = 5$, and the resulting LFR size is 20; this number represents how many times η is repeated inside the Δ block. The maximum root mean square is $9.36 \cdot 10^{-3}$, and the maximum local absolute error is $2.01 \cdot 10^{-2}$. Note that `lsapprox` instead of the orthogonal least-squares `olsapprox` routine was used because it achieves higher accuracy. The LFR order is, however, is higher but remains acceptable; that is, the computation cost for simulation using Simulink [43] is only increased by a few seconds. The resulting approximated aerodynamic gradients are plotted in Fig. 7.

IV. Integrated Design and Control

In this section, the integrated design and control problem of simultaneously minimizing the elevon's span parameter η while satisfying the handling qualities and maneuverability constraints is developed.

A. Structure of Control Laws

As stated in Sec. II.B, the longitudinal instability on this BWB requires a SAS to make it flyable. Moreover lateral control laws are also mandatory to enhance lateral handling qualities. Considering both these longitudinal and lateral/directional control laws is, moreover, necessary for a proper sizing of control surfaces. A main contribution of this paper is, indeed, to provide a methodology for simultaneous longitudinal, lateral, and directional control law's synthesis of an arbitrary structure; whereas this problem is usually addressed by decoupling longitudinal from lateral/directional axes. Here, a typical fly-by-wire FCS architecture is considered. The pilot provides inputs in terms of the commanded load factor Nz_c, bank angle ϕ_c, and sideslip β_c. Control law feedback features a C^* and Y^* structure for longitudinal and lateral/directional control, respectively, for which the structure is provided in [44]. More precisely, the following holds true:

1) The C^* structure is composed of the load factor Nz and pitch rate q feedback, together with an integrator for a zero steady-state tracking error and a direct feedthrough gain. The output of the law is an equivalent elevator order δm_{equi}.

2) The Y^* structure features lateral/directional state feedback, namely, sideslip β, yaw rate r, bank angle ϕ, and roll rate p. An integrator is added to keep zero steady-state sideslip, as well as a bank angle order direct feedthrough gain. Outputs of this law are the equivalent aileron and rudder order δl_{equi} and δn_{equi}, respectively.

A general overview of the control law structure is visible in Fig. 8. As already mentioned, control law outputs are the equivalent elevator, aileron, and rudder orders, which are independent from the

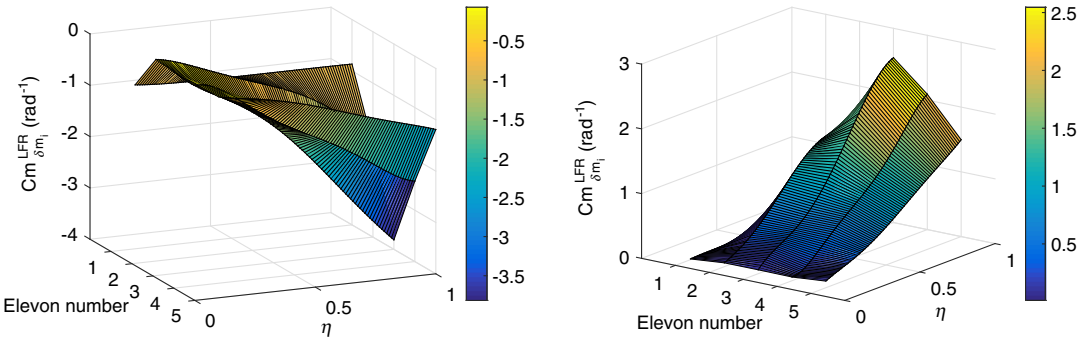

a) $Cm^{LFR}_{\delta m_i}$ approximation of elevon pitch gradient for varying η

b) $Cl^{LFR}_{\delta m_i}$ approximation of elevon roll gradient for varying η

Fig. 7 LFR polynomial approximations of elevon pitch and roll gradients.

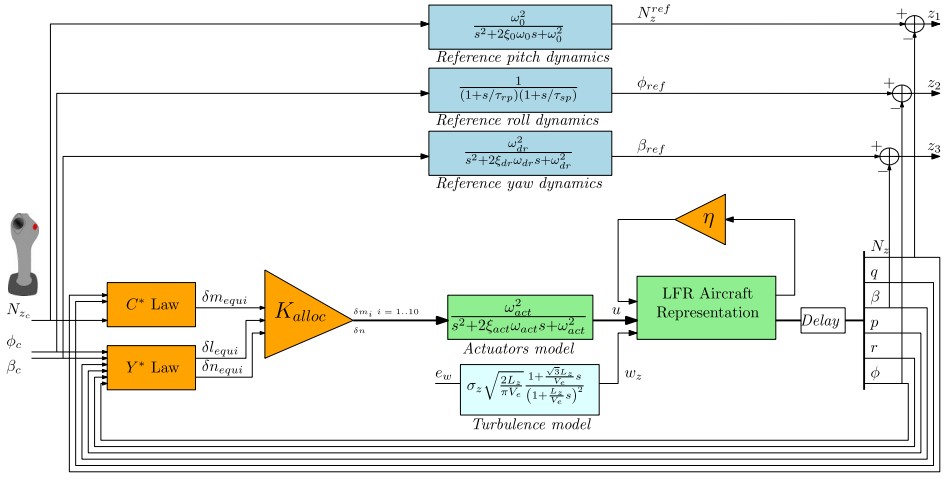

Fig. 8 Closed-loop representation for integrated design and control optimization.

control surface's architecture. These equivalent orders are then converted into control surface deflections, thanks to a control allocation module, which is described in the next section.

B. Control Allocation Model

Control allocation is the problem of converting equivalent orders, computed by the control law, into control orders when there are more effectors than axes to control. For a comprehensive survey of control allocation methods, please refer to the work by Johansen and Fossen [45]. In our study, a control allocation module needs to be incorporated in order to convert equivalent elevator, aileron, and rudder deflections ($\delta m_{\text{equi}}, \delta l_{\text{equi}}, \delta n_{\text{equi}}$) into actual control surfaces deflections ($\delta m_{i,i=1,\ldots,10}, \delta n$).

Mathematically, the control allocation problem is that of finding a deflections vector u satisfying the following:

$$\underbrace{\begin{bmatrix} Cm_{\delta m_1} & \ldots & Cm_{\delta m_{10}} & Cm_{\delta n} \\ Cl_{\delta m_1} & \ldots & Cl_{\delta m_{10}} & Cl_{\delta n} \\ Cn_{\delta m_1} & \ldots & Cn_{\delta m_{10}} & Cn_{\delta n} \end{bmatrix}}_{B_1(\eta)} \boldsymbol{u} = \begin{bmatrix} Cm_{\delta m_{\text{equi}}} \delta m_{\text{equi}} \\ Cl_{\delta l_{\text{equi}}} \delta l_{\text{equi}} \\ Cn_{\delta n_{\text{equi}}} \delta n_{\text{equi}} \end{bmatrix} \tag{19}$$

where $B_1(\eta)$ is the matrix of the elevon's gradients in pitch, roll, and yaw, respectively, which all depend on the parameter η. $[Cm_{\delta m_{\text{equi}}} Cl_{\delta l_{\text{equi}}} Cn_{\delta n_{\text{equi}}}]^T$ is a vector of equivalent gradients as seen by the control law. These values may be set arbitrarily without loss of generality; we chose equivalent values of one on all axes. Then, a classical solution of Eq. (19) is the Moore–Penrose pseudoinverse [46]:

$$\boldsymbol{u} = K_{\text{alloc}}(\eta) \begin{bmatrix} \delta m_{\text{equi}} \\ \delta l_{\text{equi}} \\ \delta n_{\text{equi}} \end{bmatrix} \tag{20}$$

with

$$K_{\text{alloc}}(\eta) = B_1^T (B_1 B_1^T)^{-1} \tag{21}$$

As comprehensively discussed in Sec. IV.C, our process features two steps. In the first step, three-axis gains are computed for a fixed η value; in this step, the pseudoinverse control allocation from Eq. (21) is used. During the second step, three-axis control law gains and the η parameter are simultaneously optimized. In this step, K_{alloc} is no longer fixed but is a variable for the optimization. By doing this, the design space is widened, and a truly optimal strategy with respect to the imposed handling qualities constraints can be chosen by the optimizer.

More precisely, in order to limit the number of variables for the optimization, K_{alloc} is parameterized as follows:

$$K_{\text{alloc}} = \begin{bmatrix} K_{\text{alloc}}^{\text{pitch}} & K_{\text{alloc}}^{\text{roll}} & 0 \\ K_{\text{alloc}}^{\text{pitch}} & -K_{\text{alloc}}^{\text{roll}} & 0 \\ 0 & 0 & K_{\text{alloc}}^{\text{yaw}} \end{bmatrix} \tag{22}$$

This means we impose symmetrical and antisymmetrical deflections of the elevons for a pitch and roll order, respectively; and a yaw order is allocated to the rudder only. By incorporating this physical knowledge of the control allocation structure, the number of variables within K_{alloc} is reduced from 33 to 11 variables.

C. Simultaneous Three-Axis Control Law Synthesis

Integrated design and control of the BWB presented in this paper follows a two-step scheme:

1) A first control law's synthesis computes gains for an arbitrarily fixed η value. The problem consists of minimizing the difference between a reference model and the closed-loop aircraft. The output of this step is the optimum value of the H_∞ criterion. This section is devoted to describing this first step.

2) The output of step 1 is used to put a constraint on the maximal value of the H_∞ criterion in order to guarantee satisfactory closed-loop behavior while optimizing the elevon's size η. This step is described extensively in the next section.

As stated previously, simultaneously optimizing the control surface's size η and control law gains requires setting a constraint, in the optimization sense, that ensures an adequate closed-loop behavior of the optimal solution. This constraint was set as a maximal admissible value of an H_∞ criterion: a value that must be computed through a first synthesis. The H_∞ criterion and its optimal value computation are described now.

A three-channel model-reference tracking scheme was used. This scheme consists of minimizing the difference between a reference dynamics model and the closed-loop aircraft, from the H_∞ norm point of view [47]. If the reference model is perfectly matched by the closed loop in the whole frequency domain, then the optimal H_∞ value is zero. However, this is practically infeasible due to physical limitations; as a consequence, the optimal value is always above zero.

Here, reference-model tracking is expressed by minimizing the H_∞ norm of a three-input three-output transfer function between pilot inputs (Nz_c, ϕ_c, β_c) and outputs (z_1, z_2, z_3) the differences between reference dynamics outputs and actual closed-loop signals (Nz, ϕ, β). For a proper definition of signals, please refer to Fig. 8. In our case, multichannel transfer has several advantages over multiple single-input single-output (SISO) transfers. First, offdiagonal terms are implicitly set to zero. Hence, the resulting control law will totally decouple all three axes (namely, longitudinal from lateral/directional, but also lateral from directional), turns are performed with zero sideslip (and directional from lateral), and "pedal" inputs imply no bank. Couplings between all axes are explicitly taken into account by the control law, which a SISO approach would not. Then, this formulation is virtually independent from the open-loop model and structure of control laws. Finally, it allows for an elegant formulation of the optimization problem of Sec. IV.D: a single constraint on the H_∞ norm of this multichannel transfer ensures an adequate closed-loop behavior on all three axes. An equivalent formulation with SISO transfers would require nine constraints.

Reference models on longitudinal, lateral, and directional axes are set as follows:

$$\frac{Nz_{\text{ref}}}{Nz_c} = \frac{\omega_i^2}{s^2 + 2\xi_i \omega_i s + \omega_i^2} \tag{23}$$

$$\frac{\phi_{\text{ref}}}{\phi_c} = \frac{1}{(1 + \tau_{rp} s)(1 + \tau_{sp} s)} \tag{24}$$

$$\frac{\beta_{\text{ref}}}{\beta_c} = \frac{\omega_{dr}^2}{s^2 + 2\xi_{dr} \omega_{dr} s + \omega_{dr}^2} \tag{25}$$

In our study, the closed-loop reference values are fixed, and they are given in Table 1. Ideally, these values should depend on the open-loop dynamics, but this is left for future work.

The optimization problem for simultaneous three-axis control law synthesis simply reads as follows:

Table 1 Values for reference model

Parameter	Value
ω_i	1 rad · s^{-1}
ξ_i	0.7
τ_{rp}	1.6 s
τ_{sp}	1.9 s
ω_{dr}	0.4 rad · s^{-1}
ξ_{dr}	0.7

$$\min_{K} \left\| T_{(Nz_c,\phi_c,\beta_c)\to(z_1,z_2,z_3)}(P(\eta^{\text{init}}), K, K^{\text{init}}_{\text{alloc}}) \right\|_\infty \tag{26}$$

such that

$$\begin{aligned} &\forall\ p \in C,\ p \text{ pole of } P(s): \\ &Re(p) \le -\text{MinDecay},\ Re(p) \le -\text{MinDamping}.|p| \\ &K \text{ internally stabilizes } P(\eta) \end{aligned}$$

with K being a vector containing all control law gains defined in Sec. IV.A. The additional constraints ensure that closed-loop poles have a damping of at least 0.5 and a real part of at least 0.2. Even though those constraints may seem redundant with the reference model tracking objective, it was found that it helps the optimizer to converge.

To solve this optimization problem, the `systune` routine [48,49] from the MATLAB Robust Control Toolbox [43] was used. This routine allows tuning of fixed-order structured controllers, so it can handle physical parameter optimization combined with control gain computation. Couplings between the control and the design problem are therefore taken into account directly in a single optimization. Moreover, it is well suited to mathematical particularities of the optimization problem in Eq. (26), namely, the nonsmooth behavior of the H_∞ norm. Optima found by the algorithm are only local; consequently, several initializations should be performed in order to ensure the globality of the solution.

An example of optimized three-axis control law is shown in Figs. 9 and 10 through the frequency domain and temporal simulation responses, respectively. The chosen flight point is $M.35$, $H = 3300$ ft, and $m = 300$ T. The optimal value for the H_∞ criterion γ_∞ for this flight point, as well as the normalized constraints at the optimum $gBest$, are as follows:

$$\gamma_\infty = \left\| T_{(Nz_c,\phi_c,\beta_c)\to(z_1,z_2,z_3)}(K^{\text{opt}}) \right\|_\infty \tag{27}$$

$$\begin{aligned} &= 0.107 \\ gBest &= 0.9997 \end{aligned} \tag{28}$$

where $gBest < 1$ at the optimum means the constraints are fulfilled.

To visualize the multiaxes behavior of the resulting control law, the simulation shown in Fig. 10 features the following maneuvers:

1) At $t = 0$ s, a pilot pull up is commanded through a $\Delta Nz_c = 1g$ step order. As a result, right and left control surfaces move in a symmetric way.

2) At $t = 5\ s$, a step with a bank angle of $\phi_c = 30$ deg is commanded. Elevons start moving from their equilibrium position antisymmetrically. The Rudder is also actuated in order to maintain zero sideslip.

3) At $t = 12$ s, a $\beta_c = 5$ deg sideslip order is commanded.

The initial elevon's deflection used to trim the aircraft is not represented on Fig. 10; only variations around their initial positions are shown. To conclude this section, we emphasize the fact that the desired

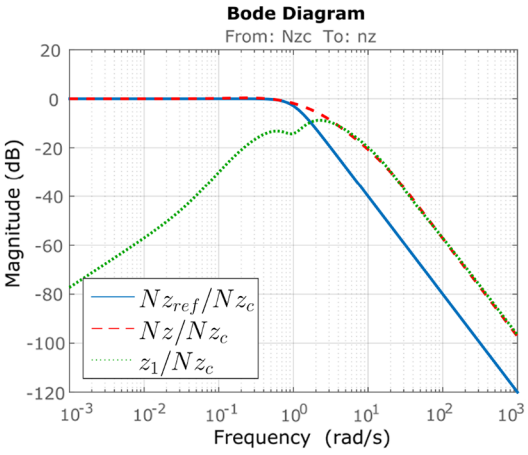

a) Comparison of longitudinal reference model, closed-loop, and error frequency responses

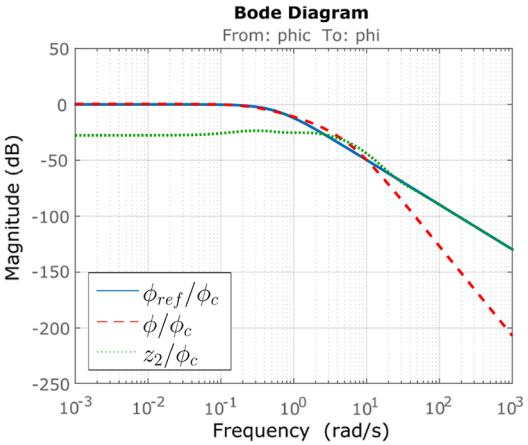

b) Comparison of lateral reference model, closed-loop, and error frequency responses

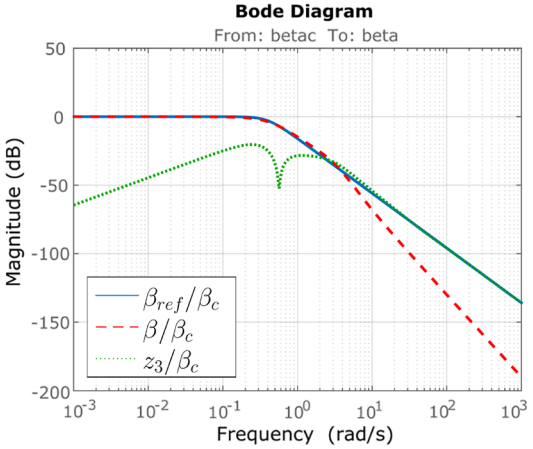

c) Comparison of directional reference model, closed-loop, and error frequency responses

Fig. 9 Bode diagrams for three-axis reference models and optimized closed loop, for $\eta = 1$.

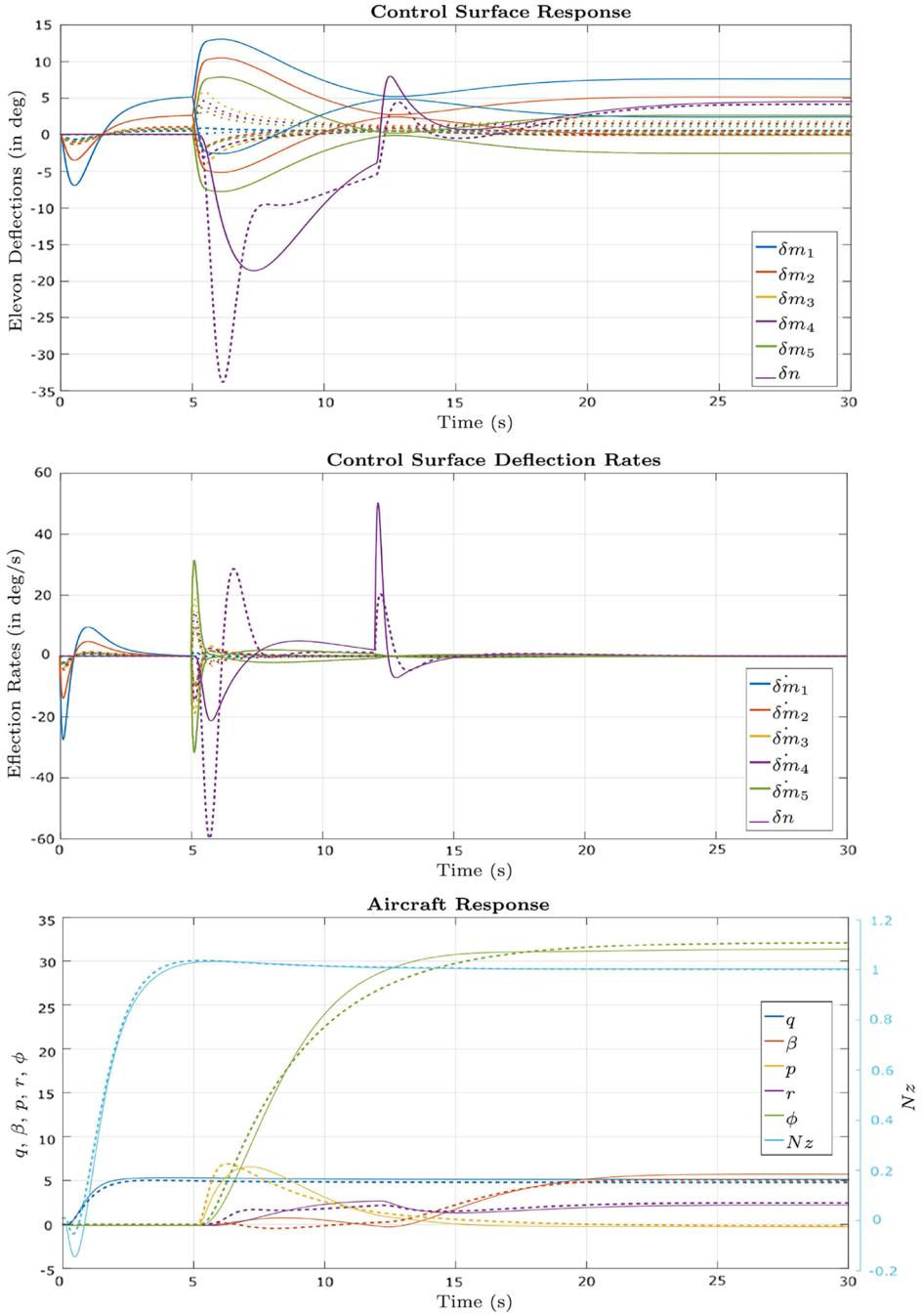

Fig. 10 Temporal responses for $\eta = 1$ (dotted lines) and $\eta^{opt} = 0.3885$ (solid lines).

outcome of the synthesis presented in this section is only the optimal value γ_∞ of the H_∞ criterion, which will be used as a constraint for the optimization procedure described in the next section. In particular, control law gains are not kept; they are computed again in the combined optimization of control laws and parameter η.

D. Definition of the Optimization Problem

Once the optimum γ_∞ of the H_∞ criterion is computed, it is used as a constraint on the H_∞ norm of the multichannel transfer for the combined optimization problem. More precisely, the integrated design and control problem of this study is that of finding a minimal η such that 1) deflections and deflection rates in response to maneuvers do not exceed prescribed limits, and 2) closed-loop behavior is optimal.

The latter point is solved by ensuring that the H_∞ norm of the multichannel transfer

$$\|T_{(Nz_c,\phi_c,\beta_c)\to(z_1,z_2,z_3)}(\eta)\|_\infty$$

is kept under its optimal value (that is, equal to this value) whatever η. Once the optimum value γ_∞ for a fixed η is known from the optimization described in Sec. IV.C, the optimization problem of finding the best possible closed-loop behavior translates into a single constraint satisfaction problem. This elegant formulation allows minimizing of another objective (η in our case) while ensuring a satisfactory closed-loop behavior on all axes.

Constraints on maneuverability are cast as constraints on the H_∞ norm of adequate transfer functions, which is similar to the work of Niewhoener and Kaminer [29]. Therefore, these constraints are root mean square and not temporal: no guarantee can be obtained in time-domain simulations. When an H_∞ handling qualities constraint is saturated, the only time-domain interpretation that can be made is that the maximum deflection is achieved for a sinusoidal input at the frequency for which the maximum H_∞ norm was computed. The reader interested in an extensive comparison between the frequency constraints and the associated time responses may refer to [50].

Having in mind these limitations, we believe this method still delivers useful information for sizing at a future project level. Moreover, it is widely used in the literature (see, for instance, [21,29,51]). Research has been done on time-domain output bounding (see, for instance, [52]); the integration of this work to our process is left for future work.

The following constraints are ensured:

1) The first constraint includes the maximum deflections and deflection rate in response to a pilot pull up. This is ensured through a constraint on the following H_∞ norms:

$$\left\| \frac{1}{\Delta\delta m_i^{\max}} T_{Nz_c \to u} \Delta N z_c^{\max} \right\|_\infty \leq 1$$

and

$$\left\| \frac{1}{\dot{\delta} m_i^{\max}} T_{Nz_c \to \dot{u}} \Delta N z_c^{\max} \right\|_\infty \leq 1$$

respectively, with $\Delta\delta m_i^{\max} = \delta m_i^{\max} - \delta m_e$.

2) The second constraint includes the maximum deflections and deflection rate in response to severe longitudinal turbulence. This is ensured through a constraint on the following H_∞ norms:

$$\left\| \frac{2}{\Delta\delta m_i^{\max}} T_{e_z \to u} \right\|_\infty \leq 1$$

and

$$\left\| \frac{2}{\dot{\delta} m_i^{\max}} T_{e_z \to \dot{u}} \right\|_\infty \leq 1$$

respectively.

3) The third constraint includes the maximum deflections and deflection rate in response to the $\phi^{\max}$ bank angle order. This is ensured through a constraint on the following H_∞ norms:

$$\left\| \frac{1}{\Delta\delta m_i^{\max}} T_{\phi_c \to u} \phi^{\max} \right\|_\infty \leq 1$$

and

$$\left\| \frac{1}{\dot{\delta} m_i^{\max}} T_{\phi_c \to \dot{u}} \phi^{\max} \right\|_\infty \leq 1$$

respectively.

Chosen values for the sizing are as follows:

1) The first value is $\delta m^{\max} = 25$ deg. A 5 deg margin versus deflection stops at 30 deg was chosen to avoid entering the nonlinear part of control authority. Please also note that, for the maximal deflection allowed, the deflection used for trim δm_e was taken into account into the computation of $\Delta\delta m^{\max}$: the more deflections are needed in order to balance the aircraft, the less authority remains available for control.

2) The second value is $\dot{\delta} m^{\max} = 60$ deg/s.

3) The third value is $\Delta N z_c^{\max} = 1.5g$.

4) The fourth value is $\phi_c^{\max} = 45$ deg.

The combined optimization problem is finally summarized in Table 2.

The process developed in this paper was extensively described in [50].

V. Results

In this section, the results of the integrated design and control process are analyzed.

Table 2 Integrated design and control optimization problem

	Function/variable	Description	Quantity
minimize	η	Outer elevon's total span	— —
with respect to	K	Control law gains	16
	K_{alloc}	Control allocation matrix	11
	η	Outer elevon's total span	1
subject to	$\left\| \frac{1}{\Delta\delta m_i^{\max}} T_{Nz_c \to u} \Delta\alpha \frac{V_e}{g} z_\alpha \right\|_\infty \leq 1$	Maximum deflection in response to longitudinal order	5
	$\left\| \frac{1}{\dot{\delta} m_i^{\max}} T_{Nz_c \to \dot{u}} \Delta\alpha \frac{V_e}{g} z_\alpha \right\|_\infty \leq 1$	Maximum deflection rate in response to longitudinal order	5
	$\left\| \frac{2}{\Delta\delta m_i^{\max}} T_{e_z \to u} \right\|_\infty \leq 1$	Maximum deflection in response to longitudinal turbulence	5
	$\left\| \frac{2}{\dot{\delta} m_i^{\max}} T_{e_z \to \dot{u}} \right\|_\infty \leq 1$	Maximum deflection rate in response to longitudinal turbulence	5
	$\left\| \frac{1}{\Delta\delta m_i^{\max}} T_{\phi_c \to u} \phi^{\max} \right\|_\infty \leq 1$	Maximum deflection in response to bank order	5
	$\left\| \frac{1}{\dot{\delta} m_i^{\max}} T_{\phi_c \to \dot{u}} \phi^{\max} \right\|_\infty \leq 1$	Maximum deflection rate in response to bank order	5
	$\left\| T_{(Nz_c, \phi_c, \beta_c) \to (z_1, z_2, z_3)} \cdot \frac{1}{\gamma_\infty} \right\|_\infty \leq 1$	Optimal closed-loop performance	1
	$\forall\ p \in C$, $p$pole of $P(s)$:	Closed-loop poles location	1
	$Re(p) \leq -\text{MinDecay}, Re(p) \leq -\text{MinDamping}.\lvert p \rvert$	— —	— —
	K internally stabilizes $P(\eta)$	— —	— —

A. Integrated Design and Control on a Single Flight Point

Integrated design and control with tunable allocation applied to the flight point of $M.35$, $H = 3300$ ft, and $m = 300T$ gives the following results:

$$\eta^{\text{opt}} = 0.3885 \tag{29}$$

$$gBest = 0.9998 \tag{30}$$

A 61% decrease in the control surfaces span is achieved as compared to the initial layout while still satisfying all handling quality constraints, i.e., $gBest < 1$. More precisely, Fig. 11, gathering all handling qualities constraints at the optimum, indicates that, on this flight point, the roll constraint is limiting. As a consequence, the optimal allocation is to distribute equally among all controls the roll order; hence, all roll criteria are equally saturated. As pitch is not limiting on this flight point, only two controls are used for pitch control. Such a strategy can also be seen on the temporal response of Fig. 10: all five controls are equally used for the roll maneuver, resulting in equal deflection rates for all controls. This behavior is confirmed by looking at the optimized allocation matrix:

$$K_{\text{alloc}}^{\text{opt}} = \begin{bmatrix} 0.023 & 0.3811 & 0 \\ 0.0116 & 0.3811 & 0 \\ 0.000 & 0.3811 & 0 \\ 0.000 & 0.3811 & 0 \\ 0.000 & 0.3811 & 0 \\ 0.023 & -0.3811 & 0 \\ 0.0116 & -0.3811 & 0 \\ 0.000 & -0.3811 & 0 \\ 0.000 & -0.3811 & 0 \\ 0.000 & -0.3811 & 0 \\ 0.000 & 0.000 & 0.006 \end{bmatrix} \tag{31}$$

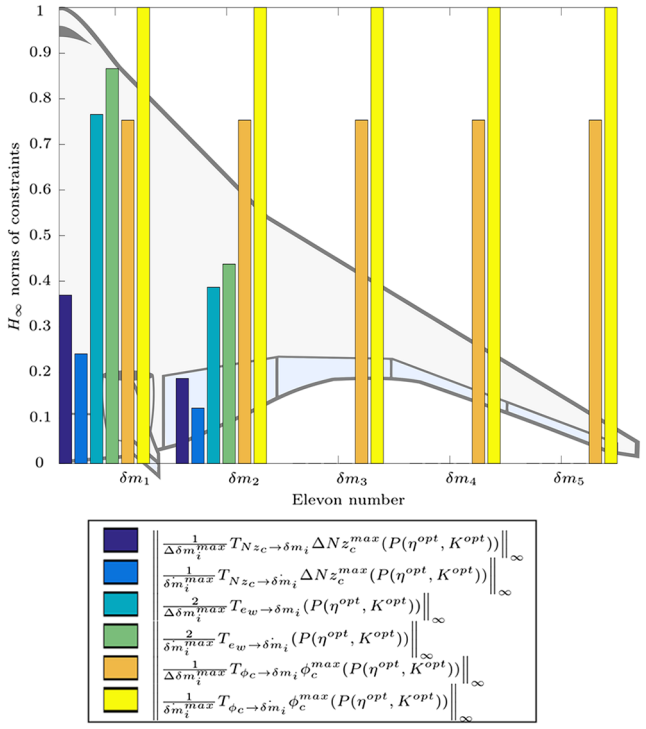

Fig. 11 Bar diagram of normalized constraint values after optimization with tunable allocation: $\eta^{\text{opt}} = 0.3885$.

B. Results on the Entire Flight Envelope

Integrated design and control with tunable allocation is now applied on the whole flight domain described in Sec. III. Figure 12 shows the resulting surface $\eta^{\text{opt}} = f(M, H)$, as well as sizing constraints associated with each optimum. The maximum value is $\eta^{\text{opt}} = 0.5996$: the aircraft can adequately be controlled on the whole flight envelope, without reaching its control stops, with only 60% of the initial control surface span. Then, the sizing values for η^{opt} (i.e., maximum values over the flight envelope) are achieved for low dynamic pressure cases: that is, low speed and high altitude. It was also shown in Sec. II.B that these cases correspond to the maximum longitudinal instability. Interestingly, those sizing points are limited by a combination of turbulence, and longitudinal and lateral maneuvers. As expected, strong stabilization to an exogenous input is definitely sizing for some specific flight points. Moreover, these results highlight the importance of the control allocation module for a correct sizing of the aircraft: it has a direct influence on the design.

VI. Conclusions

A new method for sizing the control surfaces of an unstable blended-wing–body using closed-loop handling quality criteria was presented. This method consists of simultaneously optimizing the longitudinal and lateral control laws, as well as a control allocation module, while minimizing the control surface areas under handling quality constraints. From a sizing perspective, we have shown that the

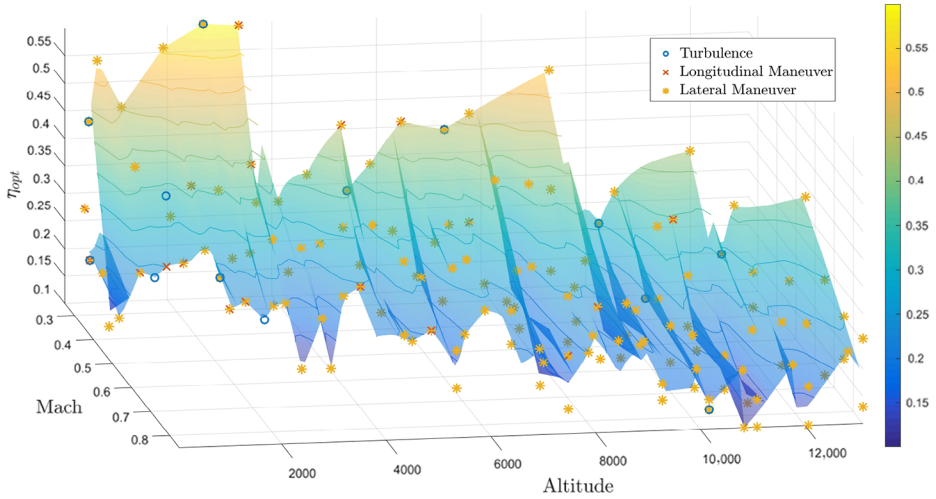

Fig. 12 η^{opt}, as a function of flight point, associated with limiting constraints.

studied Airbus blended-wing–body configuration can adequately be controlled on all three axes, on the whole flight envelope, with only 60% of the initial control surface's span, with normal laws and full control authority, with reasonable hypotheses on the actuators, sensors, and delay chain. Future work concerning the sizing of this aircraft should investigate the control authority under failure cases.

From a methodological perspective, the benefit of a simultaneous design and control approach is demonstrated: in a single step, the sizing is guaranteed with respect to the handling quality criteria, taking into account control laws. Further work should investigate temporal criteria instead of frequency (root mean square) criteria. Finally, alternative optimizers could be considered for solving this coupled problem; given the nonsmooth nature of the mathematical problem, simulation-based routines such as genetic algorithms could be worth examining.

Appendix

Developing the coefficients in state-space matrices of Sec. II.A gives the following:

$$x_V = \frac{-\rho V S C_x}{m} + \frac{\partial F}{\partial V}, \quad x_\alpha = -2\ gkC_{L_\alpha},$$
$$x_q = \frac{-2\ gLk}{V} C_{L_q}, \qquad x_\beta = -\frac{1}{2}\rho V^2 S C_{x_\beta}$$
$$z_V = \frac{-2\ g}{V^2}, \qquad z_\alpha = \frac{\rho V S}{2\ m} C_{L_\alpha},$$
$$z_q = \frac{\rho S L}{2\ m} C_{L_q}, \qquad m_\alpha = \frac{\rho V^2 S}{B} C_{m_\alpha},$$
$$m_q = \frac{\rho V S L^2}{2B} C_{m_q}, \qquad x_{\delta x} = \frac{1}{m}\frac{\partial F}{\partial \delta x},$$
$$x_{\delta m_i} = -2\ gkC_{L_{\delta m_i}}, \qquad z_{\delta m_i} = \frac{\rho V S}{2\ m} C_{L_{\delta m_i}},$$
$$m_{\delta m_i} = \frac{\rho V^2 S L}{2B} C_{m_{\delta m_i}}$$
$$y_\beta = \frac{\rho V_e S}{2m} C_{y_\beta}, \qquad y_p = \frac{\rho S L}{2m} C_{y_\beta}$$
$$y_r = \frac{\rho S L}{2m} C_{y_\beta}, \qquad y_{\delta m_i} = \frac{\rho V_e S}{2m} C_{y_{\delta m_i}}$$
$$y_{\delta n} = \frac{\rho V_e S}{2m} C_{y_{\delta n}}, \qquad \tilde{l}_\beta = \frac{\rho V_e^2 S L}{2A} \tilde{C}_{l\beta}$$
$$\tilde{l}_p = \frac{\rho V_e^2 S L}{2A} \tilde{C}_{lp}, \qquad \tilde{l}_r = \frac{\rho V_e^2 S L}{2A} \tilde{C}_{lr}$$
$$\tilde{l}_{\delta n} = \frac{\rho V_e^2 S L}{2A} \tilde{C}_{l_{\delta n}}, \qquad \tilde{n}_\beta = \frac{\rho V_e^2 S L}{2C} \tilde{C}_{n_\beta}$$
$$\tilde{n}_p = \frac{\rho V_e^2 S L}{2C} \tilde{C}_{n_p}, \qquad \tilde{n}_r = \frac{\rho V_e^2 S L}{2C} \tilde{C}_{n_r}$$
$$\tilde{n}_{\delta m_i} = \frac{\rho V_e^2 S L}{2C} \tilde{C}_{n_{\delta m_i}}, \qquad \tilde{n}_{\delta n} = \frac{\rho V_e^2 S L}{2C} \tilde{C}_{n_{\delta n}}$$

Acknowledgments

This work is part of a Ph.D. thesis in cooperation between Institut Supérieur de l'Aéronautique et de l'Espace (ISAE)-SUPAERO, ONERA—The French Aerospace Lab, and the Future Projects Office of Airbus Operations SAS.

References

[1] Liebeck, R. H., "Design of the Blended Wing Body Subsonic Transport," *Journal of Aircraft*, Vol. 41, No. 1, 2004, pp. 10–25. doi:10.2514/1.9084

[2] Martínez-Val, R., and Pérez, E., *Medium Size Flying Wings*, von Kármán Inst. for Fluid Dynamics, 2005.

[3] Qin, N., Vavalle, A., Le Moigne, A., Laban, M., Hackett, K., and Weinerfelt, P., "Aerodynamic Considerations of Blended Wing Body Aircraft," *Progress in Aerospace Sciences*, Vol. 40, No. 6, 2004, pp. 321–343. doi:10.1016/j.paerosci.2004.08.001

[4] Bolsunovsky, A., Buzoverya, N., Gurevich, B., Denisov, V., Dunaevsky, A., Shkadov, L., Sonin, O., Udzhuhu, A., and Zhurihin, J., "Flying Wing—Problems and Decisions," *Aircraft Design*, Vol. 4, No. 4, 2001, pp. 193–219. doi:10.1016/S1369-8869(01)00005-2

[5] Roman, D., Allen, J., and Liebeck, R., "Aerodynamic Design Challenges of the Blended-Wing-Body Subsonic Transport," *18th Applied Aerodynamics Conference*, AIAA Paper 2000-4335, 2000. doi:10.2514/6.2000-4335

[6] Garmendia, D. C., and Mavris, D. N., "Alternative Trim Analysis Formulations for Vehicles with Redundant Multi-Axis Control Surfaces," *Journal of Aircraft*, Vol. 53, No. 1, 2016, pp. 60–72. doi:10.2514/1.C033184

[7] Saucez, M., "Handling Qualities of the Airbus Flying Wing Resolution," Ph.D. Thesis, Institut Supérieur de l'Aéronautique et de l'Espace (ISAE)-Airbus, Toulouse, France, 2013.

[8] Saucez, M., and Boiffier, J.-L., "Optimization of Engine Failure on a Flying Wing Configuration," *AIAA Atmospheric Flight Mechanics Conference, Guidance, Navigation, and Control and Co-located Conferences*, AIAA Paper 2012-4501, 2012. doi:10.2514/6.2012-4501

[9] Roskam, J., *Airplane Design*, DARcorporation, Lawrence, KS, 1985.

[10] Garmendia, D. C., Chakraborty, I., and Mavris, D. N., "Method for Evaluating Electrically Actuated Hybrid Wing Body Control Surface Layouts," *Journal of Aircraft*, Vol. 52, No. 6, 2015, pp. 1780–1790. doi:10.2514/1.C033061

[11] Kozek, M., and Schirrer, A., *Modeling and Control for a Blended Wing Body Aircraft*, Springer, New York, 2014, pp. 29–45.

[12] Roskam, J., *Airplane Design Part VI: Preliminary Calculation of Aerodynamic, Thrust and Power Characteristics*, DARcorporation, Lawrence, KS, 1985.

[13] Roskam, J., *Airplane Flight Dynamics and Automatic Flight Controls*, DARcorporation, Lawrence, KS, 1995.

[14] Denieul, Y., Alazard, D., Bordeneuve, J., Toussaint, C., and Taquin, G., "Interactions of Aircraft Design and Control: Actuators Sizing and Optimization for an Unstable Blended Wing-Body," *AIAA Atmospheric Flight Mechanics Conference, AIAA Aviation*, AIAA Paper 2015-2553, 2015. doi:10.2514/6.2015-2553

[15] Garmendia, D. C., Chakraborty, I., and Mavris, D. N., "Multidisciplinary Approach to Assessing Actuation Power of a Hybrid Wing Body," *Journal of Aircraft*, Vol. 53, No. 4, 2016, pp. 900–913. doi:10.2514/1.C033390

[16] Wildschek, A., "Flight Dynamics and Control Related Challenges for Design of a Commercial Blended Wing Body Aircraft," *AIAA Guidance, Navigation, and Control Conference*, AIAA Paper 2014-0599, 2014. doi:10.2514/6.2014-0599

[17] Garmendia, D. C., Chakraborty, I., Trawick, D. R., and Mavris, D. N., "Assessment of Electrically Actuated Redundant Control Surface Layouts for a Hybrid Wing Body Concept," *14th AIAA Aviation Technology, Integration, and Operations Conference, AIAA Aviation*, AIAA Paper 2014-2428, 2014. doi:10.2514/6.2014-2428

[18] Fathy, H., Reyer, J., Papalambros, P., and Ulsov, A., "On the Coupling Between the Plant and Controller Optimization Problems," *Proceedings of the American Control Conference, 2001*, Vol. 3, 2001, pp. 1864–1869. doi:10.1109/ACC.2001.946008

[19] Ricardez-Sandoval, L., Budman, H., and Douglas, P., "Integration of Design and Control for Chemical Processes: A Review of the Literature and Some Recent Results," *Annual Reviews in Control*, Vol. 33, No. 2, 2009, pp. 158–171. doi:10.1016/j.arcontrol.2009.06.001

[20] Ricardez-Sandoval, L., Budman, H., and Douglas, P., "Simultaneous Design and Control of Chemical Processes with Application to the Tennessee Eastman Process," *Journal of Process Control*, Vol. 19, No. 8, 2009, pp. 1377–1391. doi:10.1016/j.jprocont.2009.04.009

[21] Silvestre, C., Pascoal, A., Kaminer, I., and Healey, A., "Plant-Controller Optimization with Applications to Integrated Surface Sizing and Feedback Controller Design for Autonomous Underwater Vehicles (AUVs)," *American Control Conference*, Vol. 3, 1998, pp. 1640–1644. doi:10.1109/ACC.1998.707284

[22] Alazard, D., Loquen, T., de Plinval, H., and Cumer, C., "Avionics/ Control Co-Design for Large Flexible Space Structures," *AIAA Guidance, Navigation, and Control (GNC) Conference, Guidance, Navigation, and Control and Co-Located Conferences*, AIAA Paper 2013-4638, 2013.
doi:10.2514/6.2013-4638

[23] Denieul, Y., Bordeneuve, J., Alazard, D., Toussaint, C., and Taquin, G., "Integrated Design and Control of a Flying Wing Using Nonsmooth Optimization Techniques," *Advances in Aerospace Guidance, Navigation and Control: Selected Papers of the Third CEAS Specialist Conference on Guidance, Navigation and Control Held in Toulouse*, edited by J. Bordeneuve-Guibé, A. Drouin, and C. Roos, Springer International Publ., Toulouse, France, 2015, pp. 475–489.
doi:10.1007/978-3-319-17518-8_27

[24] Welstead, J., and Crouse, G. L., Jr., "Conceptual Design Optimization of an Augmented Stability Aircraft Incorporating Dynamic Response and Actuator Constraints," *52nd Aerospace Sciences Meeting*, AIAA Paper 2014-0187, 2014.

[25] Perez, R., Liu, H., and Behdinan, K., "A Multidisciplinary Optimization Framework for Control-Configuration Integration in Aircraft Conceptual Design," *Journal of Aircraft*, Vol. 43, No. 6, 2006, pp. 1937–1948.
doi:10.2514/1.22263

[26] Mader, C. A., and Martins, J. R. R. A., "Stability-Constrained Aerodynamic Shape Optimization of Flying Wings," *Journal of Aircraft*, Vol. 50, No. 5, 2013, pp. 1431–1449.
doi:10.2514/1.C031956

[27] Lyu, Z., and Martins, J. R. R. A., "Aerodynamic Design Optimization Studies of a Blended-Wing–Body Aircraft," *Journal of Aircraft*, Vol. 51, No. 5, 2014, pp. 1604–1617.
doi:10.2514/1.C032491

[28] Haghighat, S., Martins, R. A., Joaquim, R., and Liu, H. H. T., "Aeroservoelastic Design Optimization of a Flexible Wing," *Journal of Aircraft*, Vol. 49, No. 2, 2012, pp. 432–443.
doi:10.2514/1.C031344

[29] Niewoehner, R. J., and Kaminer, I., "Integrated Aircraft-Controller Design using Linear Matrix Inequalities," *Journal of Guidance, Control, and Dynamics*, Vol. 19, No. 2, 1996, pp. 445–452.
doi:10.2514/3.21638

[30] Liao, F., Lum, K. Y., and Wang, J. L., "An LMI-Based Optimization Approach for Integrated Plant/Output-Feedback Controller Design," *Proceedings of the American Control Conference, 2005*, IEEE, Piscataway, NJ, 2005, pp. 4880–4885.

[31] Liao, F., Lum, K. Y., and Wang, J. L., "Mixed H2/H∞ Sub-Optimization Approach for Integrated Aircraft/Controller Design," *Proceedings of the 16th IFAC World Congress*, Prague, Czech Republic, 2005.
doi:10.3182/20050703-6-CZ-1902.01978

[32] Sridharan, S., Echols, J. A., Rodriguez, A. A., and Mondal, K., "Integrated Design and Control of Hypersonic Vehicles," *American Control Conference (ACC), 2014*, IEEE, Piscataway, NJ, 2014, pp. 1371–1376.

[33] Lhachemi, H., Saussie, D., and Zhu, G., "A Structured-Based Optimization Approach for Integrated Plant and Self-Scheduled Flight Control System Design," *Aerospace Science and Technology*, Vol. 45, Sept. 2015, pp. 30–38.
doi:10.1016/j.ast.2015.04.003

[34] Meheut, M., Arntz, A., and Carrier, G., "Aerodynamic Shape Optimizations of a Blended Wing Body Configuration for Several Wing Planforms," Vol. 10, AIAA Paper 2012-3122, 2012.
doi:10.2514/6.2012-3122

[35] Boiffier, J.-L., *The Dynamics of Flight: The Equations*, Vol. 1, Wiley, New York, 1998.

[36] Rogers, W. L., and Collins, D. J., "X-29 H-Infinity Controller Synthesis," *Journal of Guidance, Control, and Dynamics*, Vol. 15, No. 4, 1992, pp. 962–967.
doi:10.2514/3.20930

[37] Standard, M., "Flying Qualities of Piloted Aircraft," U.S. Dept. of Defense MIL-STD-1797A, 1990.

[38] Gage, S., "Creating a Unified Graphical Wind Turbulence Model from Multiple Specifications," *AIAA Modeling and Simulation Technologies Conference and Exhibit, Guidance, Navigation, and Control and Co-Located Conferences*, AIAA Paper 2003-5529, 2003.
doi:10.2514/6.2003-5529

[39] Denieul, Y., Bordeneuve, J., Alazard, D., Toussaint, C., and Taquin, G., "Integrated Design and Control of a Flying Wing Using Nonsmooth Optimization Techniques," *Advances in Aerospace Guidance, Navigation and Control*, edited by J. Bordeneuve, A. Drouin, and C. Roos, Springer International, New York, 2015, pp. 475–489.

[40] Drela, M., and Youngren, H., "AVL Aerodynamic Analysis, Trim Calculation, Dynamic Stability Analysis, Aircraft Configuration Development," 2006.

[41] Roos, C., Hardier, G., and Biannic, J.-M., "Polynomial and Rational Approximation with the APRICOT Library of the SMAC Toolbox," *2014 IEEE Conference on Control Applications (CCA)*, IEEE, Piscataway, NJ, 2014, pp. 1473–1478.
doi:10.1109/CCA.2014.6981532

[42] Zhou, K., Doyle, J. C., and Glover, K., *Robust and Optimal Control*, Vol. 40, Prentice–Hall, Upper Saddle River, NJ, 1996, Chap. 10.

[43] Robust Control Toolbox™, The MathWorks Inc., Natick, MA, 2014.

[44] Favre, C., "Fly-by-Wire for Commercial Aircraft: The Airbus Experience," *International Journal of Control*, Vol. 59, No. 1, 1994, pp. 139–157.
doi:10.1080/00207179408923072

[45] Johansen, T. A., and Fossen, T. I., "Control Allocation–A Survey," *Automatica*, Vol. 49, No. 5, 2013, pp. 1087–1103.
doi:10.1016/j.automatica.2013.01.035

[46] Bodson, M., "Evaluation of Optimization Methods for Control Allocation," *Journal of Guidance, Control, and Dynamics*, Vol. 25, No. 4, 2002, pp. 703–711.
doi:10.2514/2.4937

[47] Sima, V., *Algorithms for Linear-Quadratic Optimization*, Vol. 200, CRC Press, Boca Raton, FL, 1996, Chap. 1.

[48] Apkarian, P., "Tuning Controllers Against Multiple Design Requirements," *16th International Conference on System Theory, Control and Computing (ICSTCC)*, IEEE, Piscataway, NJ, 2012, pp. 1–6.

[49] Gahinet, P., and Apkarian, P., "Automated Tuning of Gain-Scheduled Control Systems," *IEEE 52nd Annual Conference on Decision and Control (CDC)*, IEEE, Piscataway, NJ, 2013, pp. 2740–2745.

[50] Denieul, Y., "Preliminary Design of Control Surfaces and Laws for Unconventional Aircraft Configurations," M.S. Thesis, Institut Supérieur de l'Aéronautique et de l'Espace (ISAE)-SUPAERO, Toulouse, France, 2016.

[51] Yang, G.-H., and Lum, K.-Y., "An Optimization Approach to Integrated Aircraft-Controller Design," *Proceedings of the 2003 American Control Conference*, Vol. 2, IEEE, Piscataway, NJ, 2003, pp. 1649–1654.

[52] Chambon, E., Burlion, L., and Apkarian, P., "Time-Response Shaping Using Output to Input Saturation Transformation," *International Journal of Control*, Feb. 2017, pp. 1–20.
doi:10.1080/00207179.2017.1286043